Enhanced $\vec{E} \times \vec{B}$ drift effects in the TCV snowflake divertor

G.P. Canal[1]‡, T. Lunt[2], H. Reimerdes[1], B.P. Duval[1], B. Labit[1], W.A.J. Vijvers[1] and the TCV Team[1]

[1]Ecole Polytechnique Fédérale de Lausanne (EPFL) - Centre de Recherches en Physique des Plasmas (CRPP), CH-1015 Lausanne, Switzerland
[2]Max-Planck-Institut für Plasmaphysik, Boltzmannstr. 2, 85748 Garching, Germany

E-mail: canalg@fusion.gat.com

Abstract.

Measurements of various plasma parameters at the divertor targets of snowflake (SF) and conventional single-null configurations indicate an enhanced effect of the $\vec{E} \times \vec{B}$ drift in the scrape-off layer of plasmas in the SF configuration. Plasma boundary transport simulations using the EMC3-Eirene code show that the poloidal gradients of the kinetic profiles in the vicinity of the null-point of a SF divertor are substantially larger than those of a conventional single-null configuration. These gradients are expected to drive larger $\vec{E} \times \vec{B}$ flows in the SF divertor and are thought to be responsible for the formation of the double-peaked particle and heat flux target profiles observed experimentally. Experiments in forward and reversed toroidal magnetic field directions further support this conclusion. The formation of such a double-peaked profiles is enhanced at higher plasma densities and may have beneficial effects on the divertor heat loads since they lead to broader target profiles and lower peak heat fluxes.

‡ Present address: General Atomics, P.O. Box 85608, San Diego, California 92186-5608, USA

1. Introduction

In the demonstration power plant DEMO [1], and in future tokamak-based fusion power plants, the heating power is expected to be 4-5 times higher than in ITER [2, 3]. However, as these devices will be only about 50% larger than ITER, unacceptably high values of heat flux are expected on the plasma facing components of the divertor. The solution for this problem currently relies on a combination of increased core and divertor radiation with the edge power flow sufficiently above the H-mode transition threshold. Assuming that the constraints of the DEMO divertor will be similar to those of the ITER divertor, about 70-90% of the power exhausted must be radiated inside of the last closed flux surface (LCFS) [3]. However, it is not clear if these conditions can be sustained and are compatible with the required energy confinement quality [1]. To mitigate the risk that highly radiating regimes may not extrapolate towards devices like DEMO, alternatives to the conventional divertor are being researched. One of several magnetic divertor configurations that have been proposed is the "snowflake" (SF), which is characterized by a second order null-point [4]. The SF divertor has a hexagonal structure, with four divertor legs, and a lower poloidal magnetic field in the vicinity of the null-point than a conventional single-null (SN) divertor. In practice, the currents in the poloidal field (PF) coils always differ slightly from those required for creating an exact SF configuration resulting in configurations with two nearby first order null-points. In such configurations, the primary x-point determines the LCFS. The secondary x-point can be located either in the private flux region (PFR) of the primary separatrix, referred to as snowflake plus (SF+), figure 1(a), or in its common flux region, referred to as snowflake minus (SF-) [5]. The proximity of a divertor configuration to an exact SF can be characterized by the normalized x-point separation, σ, defined as the distance between the two nearby x-points, d_{xpt}, normalized with the plasma minor radius, a.

The SF configuration is expected to reduce the wall heat loads due to its geometrical properties in the vicinity of the null-point [4, 5, 6], namely a larger divertor volume, which is usually associated with larger radiative losses and greater energy transfer to neutrals, and a longer connection length, $L_{||}$, which is usually associated with a lower electron temperature at the divertor target and easier access to detachment [7]. The SF divertor configuration was first demonstrated experimentally in the TCV tokamak [8, 9] and has since also been obtained in the NSTX spherical torus [10, 11, 12] and in the DIII-D tokamak [13]. Experiments in these devices have shown that a substantial decrease of the peak heat flux on the divertor plates can be achieved. It was also shown that the SF configuration facilitates the access to detachment [11, 13], whilst keeping the energy confinement, L-H threshold and H-mode pedestal height similar to those obtained in similarly shaped SN diverted plasmas.

In medium-sized devices, like TCV, the aforementioned enhanced geometrical properties are limited to the inner part of the scrape-off layer (SOL) closest to the separatrix [14]. In DEMO-sized devices, however, the SF properties are expected to

be enhanced across the entire SOL. Even though in TCV such enhancement occurs in a small part of the SOL, significant changes in the edge plasma transport have been observed when the divertor configuration is varied from a standard single-null to a snowflake [14, 22, 23]. These studies showed that the power distribution among strike points (SPs) and target profile shapes at secondary SPs cannot be explained by the modified field line geometry of the SF configuration alone with diffusive cross-field transport. This result strongly suggests the existence of an additional or enhanced cross-field transport in the null-point region of the SF divertor.

In this work, additional experimental measurements in the SF+ configuration and calculations using the EMC3-Eirene code are presented and compared in order to provide an improved understanding of the edge plasma transport. In the following section, the experimental setup will be presented. In section 3, the effects of σ, plasma density and direction of the toroidal magnetic field on the target profiles and power distribution among SPs are presented. In section 4, the experimental measurements are compared with EMC3-Eirene simulations. The main conclusions are summarized in section 5.

2. Experimental Setup

The experiments described in this work were carried out in Ohmicaly heated L-mode discharges with the primary x-point placed near the centre of the TCV vessel in order to clearly separate the null-point region from each of the four strike points. In these experiments, the toroidal magnetic field was set to 1.45 T and the plasma current ranges from 220 to 250 kA. Unless it is explicitly mentioned, the experiments were carried with the ion $\vec{\nabla}B$ drift directed towards the primary x-point, usually referred to as the "forward" direction of the toroidal field. The plasma density is sufficiently low to keep the divertor legs in the attached regime and thus to exhaust most of the power entering the SOL in the vicinity of the SPs [24]. The discharges were prepared using the free-boundary equilibrium code FBTE [25] that calculates the currents in the PF coils required to create a prescribed magnetic configuration. The experimental equilibria are reconstructed using the fitting code LIUQE [26].

The experimental measurements obtained in SF+ configurations, figure 1(a), are compared with those obtained from a reference configuration, defined as a SF+ configuration with $\sigma = 1.5$, figure 1(b). At such x-point separation, the location of the secondary x-point has only a negligible influence on the poloidal field and divertor configuration in the vicinity of the primary x-point. This configuration will, therefore, be referred to as SF-like SN or just SN for simplicity. In this work, the SPs in any SF configuration are labelled in a counter clock-wise direction from one to four (SP1 to SP4) starting at the highest strike point on the HFS wall of TCV. In the SF+ configuration, SP1 and SP4 are the primary SPs while SP2 and SP3 are in the PFR, figure 1(a).

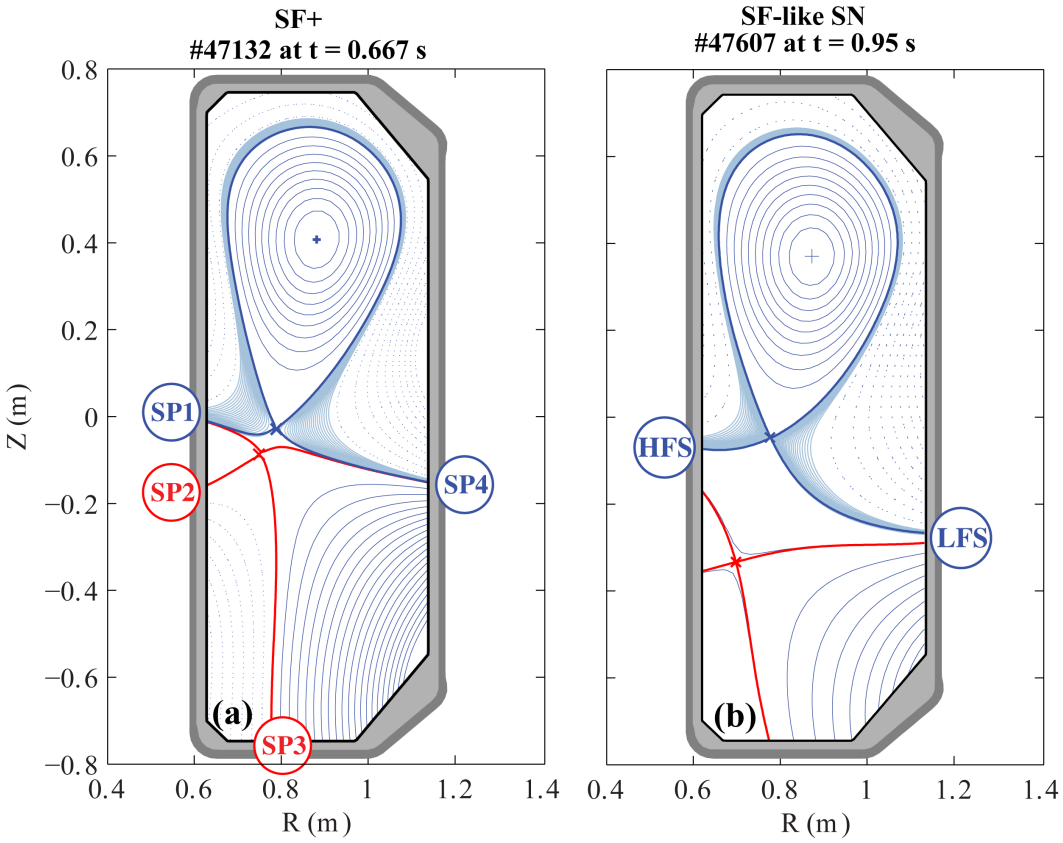

Figure 1. Typical configurations used in this work: (a) SF+ (σ = 0.25) and (b) SF-like SN (σ = 1.5) configurations.

3. Experimental Observations

In this section, the measurements at the divertor targets are presented and the effects of the normalized x-point separation, σ, line averaged electron density, $\langle n_e \rangle$, and direction of the toroidal magnetic field, B_ϕ, on the target profiles and power distribution among SPs are discussed. The target profiles are shown with respect to the reconstructed position of the separatrix using LIUQE. The target profiles at all four SPs of the SF configuration are measured by wall mounted Langmuir probes. Small sweeps of the SP position across multiple Langmuir probes, with typical duration of 250 to 300 ms, were used to increase the experimental spatial resolution.

3.1. Effect of σ on the target profiles shape

Previous TCV experiments have shown an increase of the power distribution to the secondary SPs of a SF+ when the distance between x-points decreases [14]. This enhanced power distribution is accompanied by changes in the shape of the target profiles at the primary SP1 that cannot be explained by modifications of the field line geometry alone. When σ decreases, the conventional single-peaked plasma density, n, profile at SP1 is replaced by a double-peaked profile, figure 2(a). Decreasing σ also affects the

electron temperature, T_e, profile at SP1, which becomes more peaked near the separatrix and with lower values in the far-SOL, compared with those in a SN configuration, figure 2(b). The shape of the target profiles at SP4 are not substantially affected when σ decreases.

Experimental observations of double-peaked target profiles have already been reported in conventional single-null configurations [27, 28]. A possible explanation arises from the similarities between experimental observations in JET and modelling, using the EDGE2D code with particle drifts included [29]. This study shows that the appearance of double-peaked target profiles can be caused by plasma transport due to the $\vec{E} \times \vec{B}$ drift. In a more recent work, where the effects of the $\vec{E} \times \vec{B}$ drift and parallel currents on divertor asymmetries are investigated [30], double-peaked plasma density profiles are also observed in B2SOLPS5.2 simulations of MAST plasmas when particle drifts are introduced in the calculations. These results suggest that the $\vec{E} \times \vec{B}$ drift could have a particular strong effect in the TCV SF plasmas.

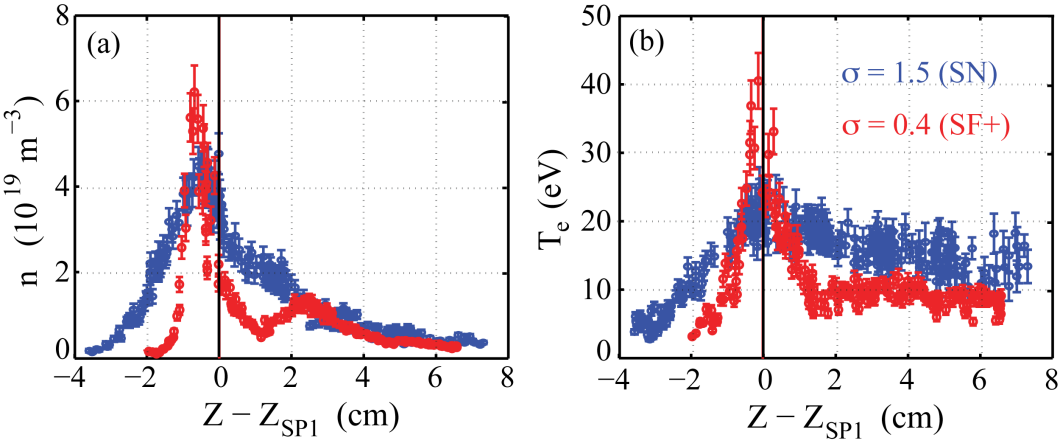

Figure 2. Langmuir probes measurements of (a) the plasma density, n, and (b) electron temperature, T_e, target profiles at SP1 in a SN ($\sigma = 1.5$) and in a SF+ configuration ($\sigma = 0.4$) both with $\langle n_e \rangle \approx 3{\times}10^{19}\,\mathrm{m}^{-3}$.

3.2. Effect of the plasma density on the power distribution among SPs and target profiles shape

The plasma density is an important parameter that determines the divertor regime. In this work, the line averaged plasma density is varied from $\langle n_e \rangle \approx 2.0$ - $9.0{\times}10^{19}$ m^{-3} in order to characterize the SOL regime and thus the importance of particle drifts on the edge plasma transport.

Langmuir probe measurements of the recycling current show that SP1 remains attached for $\langle n_e \rangle \lesssim 7.0{\times}10^{19}$ m^{-3} in both forward and reversed B_ϕ directions, figure 3, and SP4 remains attached for the entire range of $\langle n_e \rangle$. The SOL regimes investigated in this work, therefore, are the sheath-limited and high-recycling regimes.

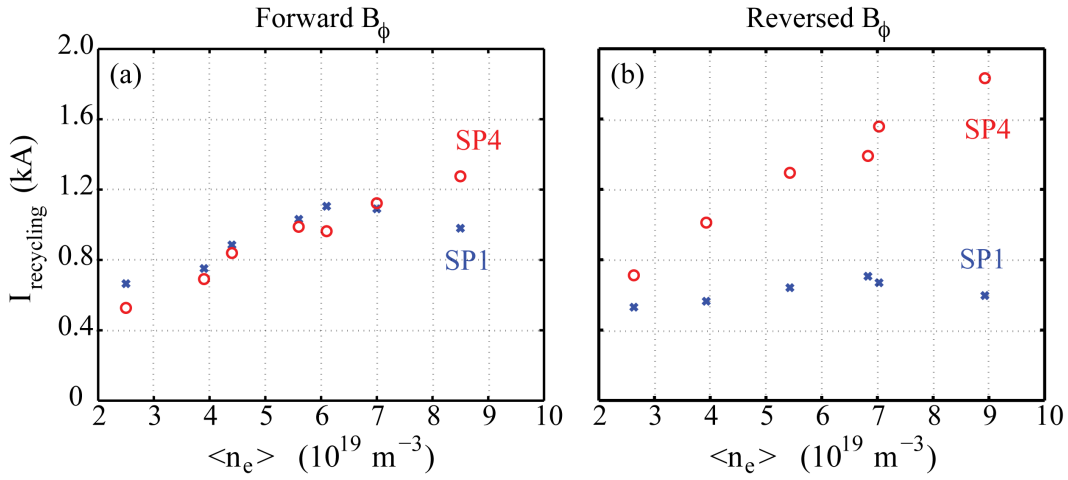

Figure 3. Langmuir probe measurements of the recycling current measured at the SP1 and SP4 targets of a SF+ configuration with $\sigma = 0.4$ in (a) forward and (b) reversed B_ϕ direction.

Gradients of the plasma kinetic profiles are the main drive for particle drifts and are expected to be stronger in the high-recycling regime and weaker in both the sheath-limited and detached regimes [31]. At lower values of $\langle n_e \rangle$, in which particle drifts are not expected to be significant, target ion saturation current, J_{sat}, and heat flux, q_t, measurements at SP1 of the SF+ configuration show profiles with single-peaked shapes, figure 4(a) and (d), respectively. As $\langle n_e \rangle$ increases and the SOL regime changes toward the high-recycling regime, this primary peak decreases in amplitude and a second peak arises on the SOL side of the primary peak, suggesting that particle drifts start to become important, figure 4(b-c) and (e-f). The measurements also show that, along with the appearance of a second peak, these target profiles broaden, which leads to a decrease of the peak heat flux on the divertor plates. For $\langle n_e \rangle \gtrsim 5{\times}10^{19}\,\mathrm{m}^{-3}$, the amplitude of the second peak exceeds the amplitude of the primary peak and, for even higher values of $\langle n_e \rangle$, the second peak dominates the profile shape changing it back to single-peaked again. Note that the location of the second peak is not fixed in space since the SPs were swept cross many Langmuir probes to obtain the high spatial resolution measurements shown in figures 2, 4 and 6.

The power detected at the secondary strike points SP2 and SP3 decreases with increasing $\langle n_e \rangle$, figure 5. This suggests that the plasma transport responsible for the appearance of the double-peaked profiles at the SP1 target also leads to less cross-field transport into the PFR.

3.3. Effect of the direction of B_ϕ on the target profiles shape

Since a possible explanation for the observed shape of the target profiles in SF+ configurations is based on particle drifts [29, 30], reversing the direction of B_ϕ is expected to have a significant effect on the edge plasma transport and on the shape of the target

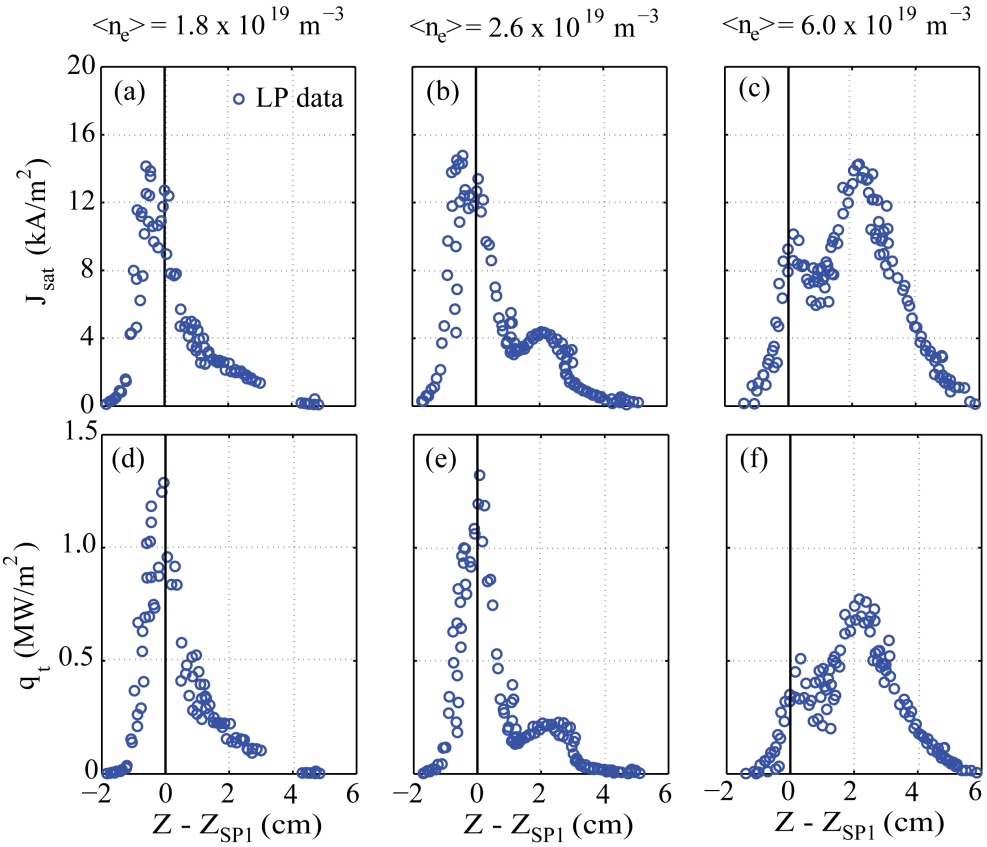

Figure 4. Ion saturation current, $J_{\rm sat}$, measured across the SP1 divertor target of a SF+ configuration with $\sigma = 0.4$ and line averaged plasma density (a) $\langle n_{\rm e}\rangle = 1.8{\times}10^{19}$ m^{-3}, (b) $\langle n_{\rm e}\rangle = 2.6{\times}10^{19}$ m^{-3} and (c) $\langle n_{\rm e}\rangle = 6.0{\times}10^{19}$ m^{-3}. (d-f) Heat flux, $q_{\rm t}$, profiles corresponding to the $J_{\rm sat}$ profiles shown in (a-c), respectively.

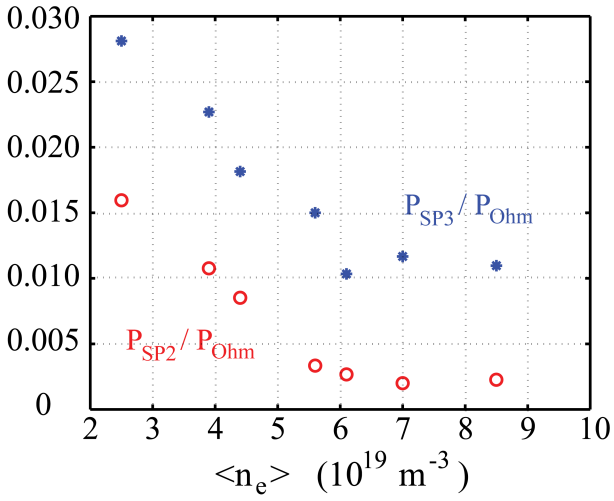

Figure 5. Langmuir probe measurements showing the dependence of the power distribution to SP2 and SP3 as a function of line averaged plasma density, $\langle n_{\rm e}\rangle$, in a SF+ configuration with $\sigma = 0.35$.

profiles [31]. Corresponding experiments with reversed B_ϕ were carried out and the measurements show that the double-peaked plasma density profile in forward B_ϕ is replace by a conventional single-peaked profile in reversed B_ϕ, figure 6(a). In addition, the primary peak of the plasma density profile in forward B_ϕ occurs in the PFR side of SP1 whereas, in reversed B_ϕ, it occurs in the SOL side. Reversing B_ϕ also affects the electron temperature profile, figure 6(b). The peaked profile near the separatrix, observed in forward B_ϕ, is replaced by a flatter profile when B_ϕ is reversed. In reversed B_ϕ, Langmuir probe measurements of the plasma density profiles at SP1 show standard single-peaked profile shapes for the entire range of investigated $\langle n_e \rangle$ and no significant change in shape has been observed. This dependence on the direction of B_ϕ further supports the hypothesis that particle drifts have a significantly stronger influence on the plasma edge transport in the SF+ configuration than in a standard SN configuration. While the target profiles at SP1 are sensitive to the direction of B_ϕ, no significant changes on the target profile shapes are observed at SP4 when B_ϕ is reversed.

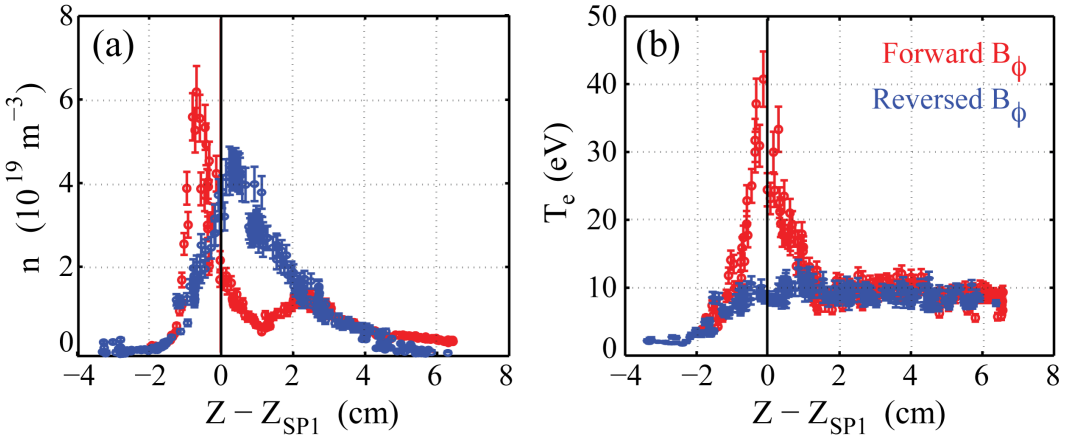

Figure 6. Langmuir probe measurements of (a) the electron plasma density and (b) temperature at the SP1 in forward and reversed B_ϕ direction, for $\langle n_e \rangle \approx 3{\times}10^{19}\,\mathrm{m}^{-3}$.

4. EMC3-Eirene Simulations of the SF+ configuration

The EMC3-Eirene code is used to interpret the experimental observations presented in section 3 and provide a better insight into the physical processes involved in the plasma transport and power distribution among SPs in both the SF+ and standard divertor configurations.

4.1. The EMC3-Eirene code

The edge Monte Carlo 3D (EMC3) code [15, 16, 17] is a steady state model of the edge plasma transport based on a fluid approach. It solves Braginskii's fluid equations [18] using a Monte Carlo technique in real space and a field-aligned local orthogonal vector basis [16, 15]. The dynamics of the neutral particle production and transport are

modelled using the Eirene code [19] and are treated with a kinetic approach, where the Fokker-Planck equation is solved and coupled self-consistently with EMC3. Although the present version of EMC3-Eirene does not account for volumetric recombination, drifts and flux limiters, recent benchmarks for standard divertor configurations have shown reasonably good agreement between EMC3-Eirene and 2D fluid codes, such as SOLPS [20] and EDGE2D-Eirene [21]. The motivation for the use of a 3D code to model a toroidally symmetric configuration such as the SF divertor is purely technical, since it simplifies the computational grid construction [23].

Previous studies using the EMC3-Eirene code to model the plasma transport in the edge of SF+ configurations showed that the power distribution to secondary SPs increases when the distance between primary and secondary separatrices decreases [23], which is in agreement with experimental observations [14]. However, these calculations underestimated the particle and heat flux at the secondary SP3 by more than one order of magnitude and do not reproduce the shape of the SP3 target profiles. The modified field line geometry of the SF divertor along with diffusive cross-field transport is, therefore, insufficient to describe the experiments, indicating the importance of an additional or enhanced transport channel for particle and heat transport across the primary separatrix. One possible explanation for the discrepancies between the simulations and experimental measurements is the absence of particle drifts in the EMC3 model that, as discussed in section 3, might have a significant effect on the plasma transport in the edge of SF+ configurations.

4.2. Description of the particle drifts

The effect of particle drifts can be investigated using a fluid or an average guiding centre approach [31]. In the fluid approach, the single-fluid momentum conservation equation yields the total particle flux, which under stationary conditions, is given by [32]

$$\vec{\Gamma} = n\,\vec{u}_{||} + \frac{\vec{f}_{\text{fric}} \times \vec{B}}{e\,B^2} + \frac{\vec{B} \times \vec{\nabla} p_{\perp}}{e\,B^2} + \\ + \frac{\left(p_{||} - p_{\perp} + n\,m_i\,u_{||}\right)}{e\,B^3}\,\vec{B} \times \left[\left(\vec{B} \cdot \vec{\nabla}\right)\frac{\vec{B}}{B}\right] + n\,\frac{\vec{E} \times \vec{B}}{B^2}. \qquad (1)$$

In this equation, n is the plasma density, $\vec{u}_{||}$ is the parallel fluid velocity, e is the elementary electric charge, m_{i} is the ion mass, $\vec{E}$ is the total self-consistent electric field, $\vec{f}_{\text{fric}}$ is a friction force density due to electron-ion collisions, $p_{||}$ is the parallel plasma pressure and $p_{\perp}$ the perpendicular plasma pressure (see [32] for more details). The parallel and perpendicular directions are defined with respect to the total magnetic field, $\vec{B}$. In equation 1, the first term represents the usual parallel particle flux while the others represent the particle transport due to various particle drifts. The second term accounts for the cross-field transport due to electron-ion collisions and is usually much smaller than the other drift terms. The third term represents the diamagnetic drift,

which do not significantly influence the plasma transport to the targets since it is largely divergence-free. The fourth term accounts for the contribution from both the curvature and gradient of the total magnetic field, which scales inversely with the major radius. The last term corresponds to the $\vec{E} \times \vec{B}$ drift and, as it scales with the local scale length of the kinetic profiles, it is usually the dominant drift term[34]. The effect of particle drifts in the null-point region of conventional SN divertor configurations, in particular the $\vec{E} \times \vec{B}$ drift, was already investigated numerically [34, 35] and experimentally [36, 37]. Since the $\vec{E} \times \vec{B}$ is the leading order term among the other drift terms, only its effect will be considered in the following analysis of the plasma transport in the SOL of SF+ configurations.

In this work, the effect of the $\vec{E} \times \vec{B}$ drift is described using a coordinate system (ρ, s_θ, ϕ) with the radial direction, $\hat{e}_\rho$, being perpendicular to the flux surfaces and the poloidal direction, $\hat{e}_\theta$, parallel to the flux surfaces in the poloidal plane, figure 7. The toroidal direction, $\hat{e}_\phi$, remains as usual.

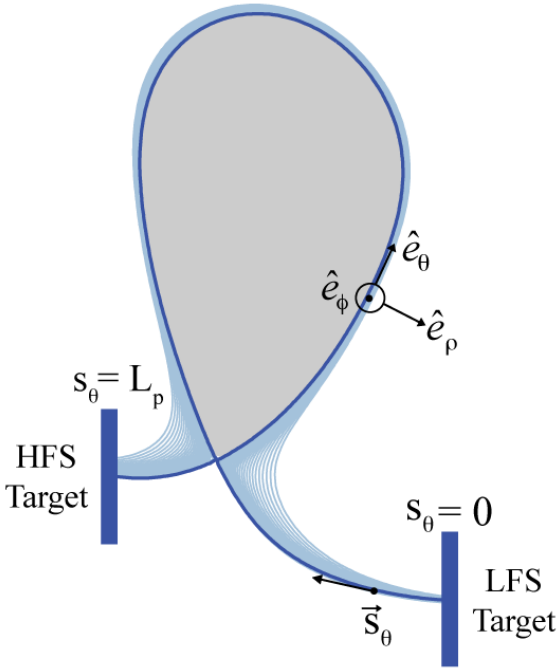

Figure 7. (ρ, s_θ, ϕ) coordinate system used to describe the $\vec{E} \times \vec{B}$ transport.

In this coordinate system, the steady state electric field, $\vec{E} = E_\rho \hat{e}_\rho + E_\theta \hat{e}_\theta + E_\phi \hat{e}_\phi$, and magnetic field, $\vec{B} = B_\theta \hat{e}_\theta + B_\phi \hat{e}_\phi$, are used to evaluate the $\vec{E} \times \vec{B}$ drift velocity,

$$\vec{u}_{\mathrm{E\times B}} = \frac{(E_\theta B_\phi - E_\phi B_\theta)}{B^2}\hat{e}_\rho - \frac{E_\rho B_\phi}{B^2}\hat{e}_\theta + \frac{E_\rho B_\theta}{B^2}\hat{e}_\phi. \tag{2}$$

The toroidal component of the electric field, $E_\phi = V_{\mathrm{loop}}/(2\pi R)$ is determined by the loop voltage, V_{loop}, with R being the major radius. The poloidal component of the electric field, $E_\theta = E_{||} B/B_\theta$, can be calculated using the parallel electron momentum

balance equation,

$$E_{||} = \frac{J_{||}}{\sigma_{||}} - 1.71\,\frac{\partial T_\mathrm{e}}{\partial s_{||}} - \frac{T_\mathrm{e}}{n}\,\frac{\partial n}{\partial s_{||}}. \tag{3}$$

Here, $E_{||}$ is the parallel electric field, $J_{||}$ is the parallel electric current density, $\sigma_{||}$ is the parallel plasma electric conductivity and $s_{||}$ is a coordinate in the parallel direction. Estimates of $E_{||}$ using equation 3 show that the $J_{||}/\sigma_{||}$ term is negligible when compared with the other terms. To estimate the importance of the $\vec{E} \times \vec{B}$ drift on the edge plasma transport, the particle flux calculated by EMC3-Eirene, $\vec{\Gamma}_{||}$, is compared with the particle flux induced by the $\vec{E} \times \vec{B}$ drift, $\vec{\Gamma}^{E\times B}$, which is estimated using the kinetic profiles calculated by EMC3-Eirene. According to equation 2, the radial component of the $\vec{E} \times \vec{B}$ drift velocity depends on the poloidal electric field that, by neglecting the parallel current and using the relation $\frac{\partial}{\partial s_{||}} = \frac{B_\theta}{B}\frac{\partial}{\partial s_\theta}$, can be calculated self-consistently:

$$E_\theta\left(\rho, s_\theta\right) = -1.71\,\frac{\partial T_\mathrm{e}\left(\rho, s_\theta\right)}{\partial s_\theta} - \frac{T_\mathrm{e}\left(\rho, s_\theta\right)}{n\left(\rho, s_\theta\right)}\,\frac{\partial n\left(\rho, s_\theta\right)}{\partial s_\theta}. \tag{4}$$

After calculating E_θ, the plasma potential Φ can be estimated by

$$\Phi\left(\rho, s_\theta\right) = \frac{T_\mathrm{e}\left(\rho, 0\right)}{2}\,\ln\left\{\frac{m_\mathrm{i}}{2\pi\, m_\mathrm{e}}\left[1 + \frac{T_\mathrm{i}\left(\rho, 0\right)}{T_\mathrm{e}\left(\rho, 0\right)}\right]^{-1}\right\} - \int_0^{s_\theta} E_\theta\left(\rho, s'_\theta\right)\, ds'_\theta. \tag{5}$$

The first term on the right hand side of equation 5 is the sheath potential across the LFS target ($\mathrm{s}_\theta = 0$) [38]. Since ambipolar transport is assumed in EMC3, the sheath potential across the HFS target could also be used instead to calculate the plasma potential, $\Phi\left(\rho, s_\theta\right)$, without affecting the result. With $\Phi\left(\rho, s_\theta\right)$, the radial electric field can be calculated, $E_\rho\left(\rho, s_\theta\right) = -\vec{\nabla}\Phi \cdot \hat{e}_\rho$.

As an example, the electric potential, and the poloidal and radial electric fields in the common flux region of a SF+ configuration with $\sigma = 0.1$ are shown in figure 8(a-c). These calculations were performed using the plasma density and electron temperature poloidal distributions from previous EMC3-Eirene simulations of the TCV discharge #43418 [23].

4.3. The relevance of the $\vec{E} \times \vec{B}$ drift in the snowflake configuration

Assuming a constant plasma background, the particle flux driven by the $\vec{E} \times \vec{B}$ drift, $\vec{\Gamma}^{E\times B} = n\,\vec{u}_{\mathrm{E\times B}}$, can be estimated from equation 2 and compared with the poloidal projection of the parallel particle flux calculated by EMC3-Eirene, $\Gamma_\theta = \Gamma_{||}\, B_\theta/B$. In this investigated case, the particle fluxes Γ_θ, $\Gamma_\rho^{E\times B}$ and $\Gamma_\theta^{E\times B}$ are of the same order of magnitude in some regions of the SOL, figures 8(d-e). The radial component of $\vec{\Gamma}^{E\times B}$ is larger than Γ_θ in the null-point region and its poloidal component is larger than Γ_θ in almost the entire SOL. In a self-consistent model, however, the parallel particle flux, $\Gamma_{||}$, would respond to this driven $\vec{E} \times \vec{B}$ flux causing significant changes in the kinetic profiles of plasma density and temperature. Since EMC3 does not take into

account the effect of particle drifts, the approach described in this work has to be seen as the first step of an iterative process towards a self-consistent solution. The absence of this convective transport mechanism in the EMC3 model could explain the observed discrepancies between simulations and experiments. In addition, the fact that this first step iteration changes the EMC3-Eirene results in the way that tends to minimize the discrepancy between simulations and experiments indicates that the $\vec{E} \times \vec{B}$ particle drift could be the missing element of the model to describe the experiments.

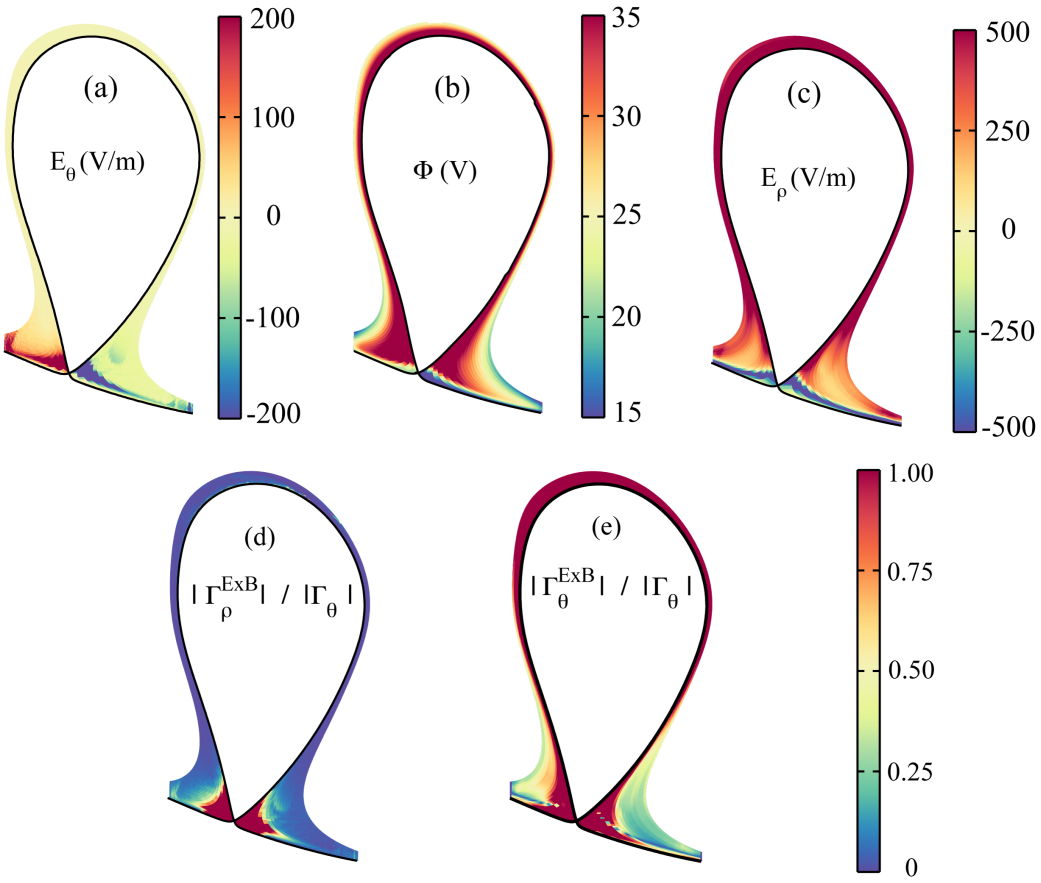

Figure 8. (a) Poloidal electric field, (b) electric potential and (c) radial electric field for a SF+ configuration with $\sigma = 0.1$. Ratio between (d) the radial and (e) poloidal component of the $\vec{E} \times \vec{B}$ particle flux with the poloidal projection of the parallel plasma flux. For these calculations, the Ohmic heating power $P_{Ohm} = 238\,\mathrm{kW}$, the plasma density at the inner simulation boundary $n = 2.5 \times 10^{19}\,\mathrm{m}^{-3}$, the cross-field particle, $D_\perp$, and heat, $\chi_\perp$, diffusivities $D_\perp = \chi_{e,\perp} = \chi_{i,\perp} = 0.6\,\mathrm{m}^2/\mathrm{s}$ (see Ref. [23] for more details).

4.4. Effect of σ on the power distribution among SPs and target profiles shape

In this section, the influence of the $\vec{E} \times \vec{B}$ drift on the plasma transport into the PFR of SF+ configurations and target profiles shape will be discussed.

According to equation 3, sufficiently large poloidal gradients of the kinetic profiles

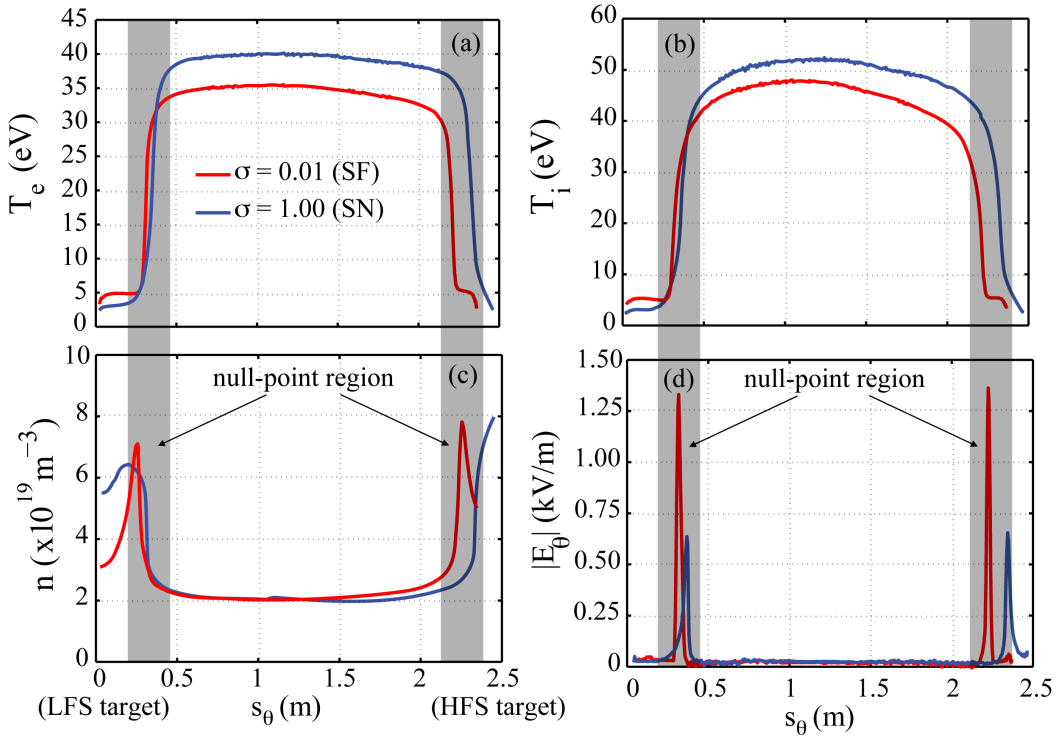

Figure 9. Poloidal profiles of the EMC3-Eirene simulated (a) electron and (b) ion temperatures, (c) plasma density and (d) poloidal electric field for a SN ($\sigma = 1.00$) and a SF+ configuration ($\sigma = 0.1$). The origin $s_\theta = 0$ corresponds to the LFS target (SP4) while the position $s_\theta = L_\mathrm{p} \approx 2.5\,\mathrm{m}$ corresponds to the HFS target (SP1).

can cause the appearance of an additional transport due to the $\vec{E} \times \vec{B}$ drift. Calculations performed using the EMC3-Eirene code show that the poloidal gradients of the kinetic profiles in the null-point region of SF+ configurations are larger compared with those in conventional SN divertors, figures 9(a-c). These larger poloidal gradients are caused by the longer parallel length of field lines within a certain poloidal interval in the null-point region of the SF divertor. The larger poloidal gradients of the kinetic profiles lead to higher values of the poloidal electric field in the null-point region, figure 9(d), which in turn are expected to cause a stronger $\vec{E} \times \vec{B}$ drift, thus leading to an additional radial transport in the SF+ configuration.

At smaller values of σ, the distance between primary and secondary separatrices decreases and a larger fraction of heat and particles transported across the primary separatrix (SP4 divertor leg) is also able to cross the secondary separatrix, figure 10(a). This effect is enhanced by the $\vec{E} \times \vec{B}$ drift as its radial component depends on E_θ, which is expected to increase when σ is reduced. Assuming a constant plasma background, the $\vec{E} \times \vec{B}$ particle flux is found to be more than one order of magnitude larger in the null-point region of the SF+ configuration than for a standard SN and, therefore, the analysis will focus in the SF+ configuration form here.

After crossing the secondary separatrix (SP4 divertor leg) in a SF+, the particles are convected towards SP3 by the poloidal component of the $\vec{E} \times \vec{B}$ drift. This predicted

effect of the $\vec{E} \times \vec{B}$ drift is in qualitative agreement with the enhanced power distribution to SP3 observed in the experiments, which is underestimated in the EMC3-Eirene simulations. The $\vec{E} \times \vec{B}$ drift also provides an explanation for the asymmetric shape of the experimentally measured heat flux profile at SP3 in SF+ configurations, figure 10(b), while the EMC3-Eirene calculations predict a symmetric profile, figure 4 of [23].

The $\vec{E} \times \vec{B}$ flow along the SP3 divertor leg is expected to enhance the plasma flow in the LFS of SP3 while on the HFS it is directed against the plasma flow. The poloidal $\vec{E} \times \vec{B}$ drift is expected to convect heat and particles from the HFS of SP3 to the lower side of SP2 while, on the upper side of SP2, the poloidal $\vec{E} \times \vec{B}$ drift transports heat and particles towards SP1, figure 10(a). This effect is also in qualitative agreement with the observed lower values of power detected at SP2, compared with those detected at SP3, and with the observation that the peak of the density profile at SP1 is located in the PFR, figure 6(a).

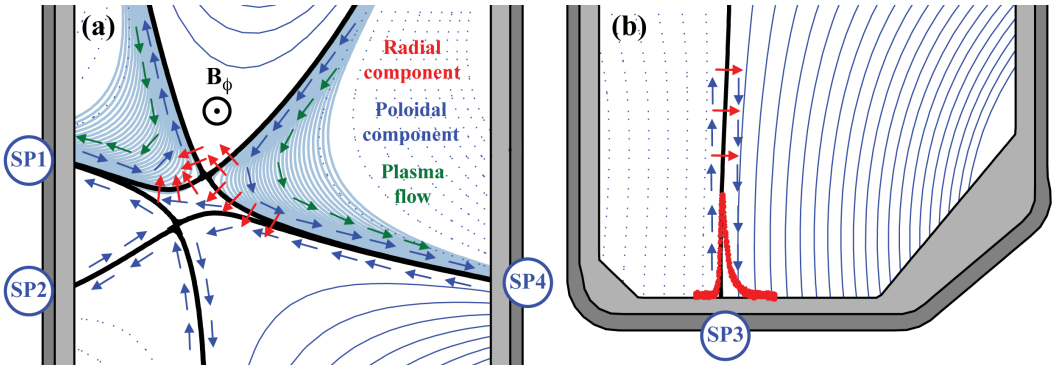

Figure 10. Schematic showing the expected $\vec{E} \times \vec{B}$ drifts (a) in the null-point region and (b) along the SP3 plasma leg of a SF+ configuration with forward toroidal magnetic field. Infrared measurements of the heat flux profile shape at SP3 are also shown in (b).

4.5. Effect of the plasma density on the power distribution among SPs

To further investigate the importance of the $\vec{E} \times \vec{B}$ drift on the activation of the secondary SPs, the radial $\vec{E} \times \vec{B}$ particle flux was calculated in the common flux region of a SF+ configuration with $\sigma = 0.1$ for two different values of plasma density. At the lower plasma density, the region with increased radial transport due to the $\vec{E} \times \vec{B}$ drift extends down to the divertor legs whereas, at the higher plasma density, the region with enhanced radial transport moves upstream, figure 11. The plasma transport across the SP4 divertor leg into the PFR due to the $\vec{E} \times \vec{B}$ drift is, therefore, expected to decrease as the plasma density increases, which agrees with the measurements shown in figure 5. The experimental measurements also show that, for $\langle n_e \rangle \gtrsim 6 \times 10^{19}$ m^{-3}, the power distribution to SP2 and SP3 becomes independent of density, which could be explained by the diminishing importance of the $\vec{E} \times \vec{B}$ drift for the transport into the PFR at higher values of plasma density. The relatively smaller power distribution to secondary

SPs observed experimentally at higher values of plasma density could be provided by, for example, diffusive transport.

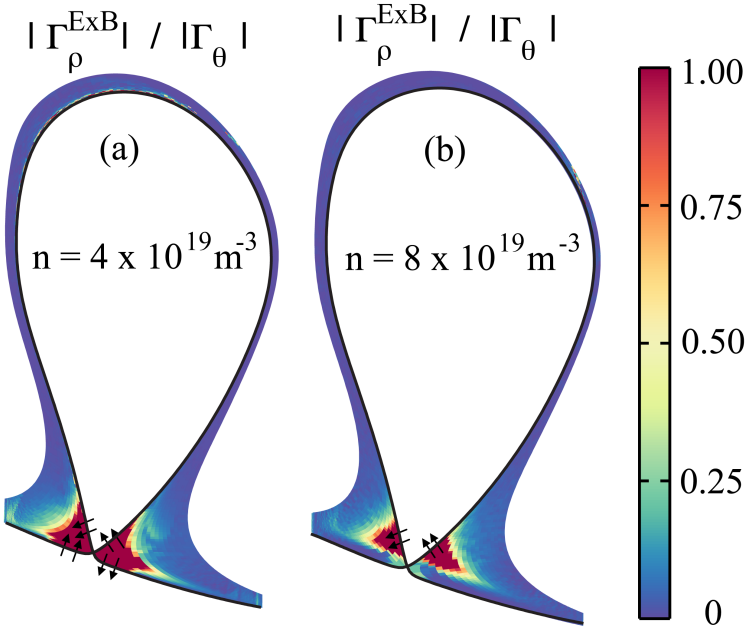

Figure 11. Ratio between the calculated radial $\vec{E} \times \vec{B}$ particle flux and the poloidal projection of the EMC3-Eirene parallel particle flux in a SF+ configuration with $\sigma = 0.1$ and forward B_ϕ for (a) $n = 4 \times 10^{19}$ m^{-3} and (b) $n = 8 \times 10^{19}$ m^{-3}.

4.6. Effect of the direction of B_ϕ on the target profiles shape

In a fluid model, the net transport caused by the $\vec{E} \times \vec{B}$ drift can be treated as source terms. In the particle conservation equation, such a source term accounts for the net particle transport caused by the divergence of the $\vec{E} \times \vec{B}$ particle flux, $S_{\mathrm{p}}^{\mathrm{E\times B}} = -\vec{\nabla} \cdot \left(\vec{\Gamma}^{\mathrm{E\times B}} \right)$. The same procedure is performed on the electron and ion energy conservation equations by adding an energy source term that corresponds to the net energy transported by the divergence of the electron ($\alpha = e$) and ion ($\alpha = i$) $\vec{E} \times \vec{B}$ energy flux, $S_{e\alpha}^{\mathrm{E\times B}} = -\vec{\nabla} \cdot \left(\frac{5}{2} k_{\mathrm{B}} T_\alpha \vec{\Gamma}_\alpha^{\mathrm{E\times B}} \right)$. In order to investigate the effects caused by the $\vec{E} \times \vec{B}$ drift on the shape of the target profiles, these source terms were calculated for a SF+ configuration with $\sigma = 0.1$ and with forward B_ϕ. The calculations show that the $\vec{E} \times \vec{B}$ drift is predicted to have a stronger effect in front of the SP1 target than in front of the SP4 target, figure 12. This is consistent with the fact that the target profile shapes at SP4 are not significantly affected by changing σ, plasma density or by reversing B_ϕ. The calculations also show that the $\vec{E} \times \vec{B}$ drift reduces the particle source, $S_{\mathrm{p}}^{\mathrm{E\times B}}$, near the separatrix in front of SP1 and increase it in the far-SOL, figure 12(a). This in turn causes a decrease of the plasma density near the separatrix in front of the SP1 target and an increase in the far-SOL, which agrees qualitatively with the double-peaked profile shapes observed at SP1, figures 2(a) and 4. Concerning the total

energy source, $S_{ee}^{\mathrm{E\times B}} + S_{ei}^{\mathrm{E\times B}}$, the calculations show that the $\vec{E} \times \vec{B}$ drift is expected to increase the amount of heat deposited near the separatrix in front of the SP1 target and reduce it in the far-SOL, figure 12(b). This would cause the electron temperature profile to peak near the separatrix at the SP1 target, which is also observed experimentally, figure 6(b).

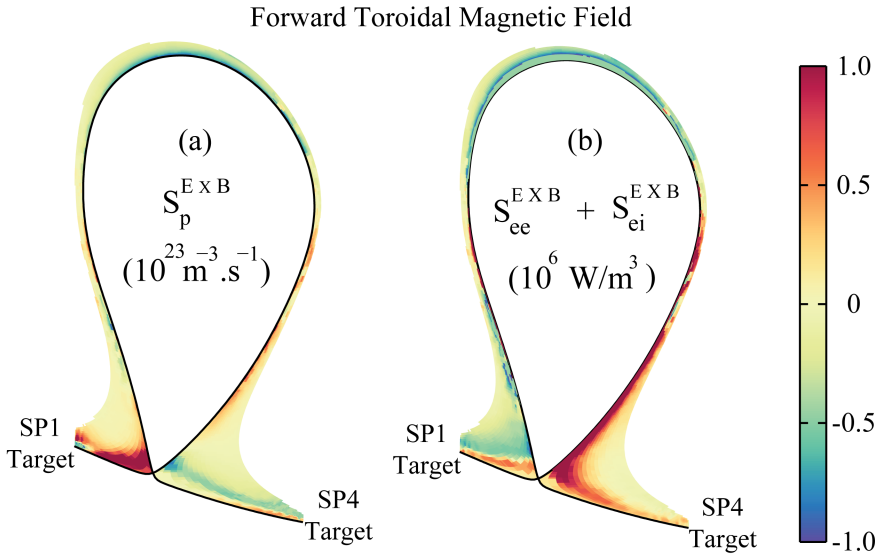

Figure 12. (a) Particle and (b) energy sources due to $\vec{E} \times \vec{B}$ drift for a SF+ configuration with $\sigma = 0.1$ and forward B_ϕ.

To further investigate the importance of the $\vec{E} \times \vec{B}$ drift on the edge plasma transport in SF+ configurations, the particle and energy sources were calculated assuming a reversed B_ϕ and compared with the experimental measurements. In reversed B_ϕ, the $\vec{E}\times\vec{B}$ drift is expected to increase the particle source, $S_{\mathrm{p}}^{\mathrm{E\times B}}$, near the separatrix in front of the SP1 target and reduce it in the far-SOL, figure 13(a). This would cause the plasma density profile at the SP1 target to have a conventional single-peaked shape rather than a double-peaked shape, which is in agreement with the measurements shown in figure 6(a). The $\vec{E}\times\vec{B}$ drift in reversed B_ϕ is also expected to reduce the total energy source, $S_{ee}^{\mathrm{E\times B}}+S_{ei}^{\mathrm{E\times B}}$, near the separatrix in front of the SP1 target and increase it in the far-SOL, figure 13(b), causing a flattening of the electron temperature profile at the SP1 target rather than a peaking, which was also observed in the experiments, figure 6(b). In addition, the calculations show that the $\vec{E} \times \vec{B}$ drift in reversed B_ϕ is expected to increase the particle source in the LFS part of the SOL and decrease it in the HFS part of the SOL with respect to the forward B_ϕ configuration. This would cause an increase of the recycling current at SP4 and a decrease of it at SP1 in reversed B_ϕ, compared with the values measured in forward B_ϕ. These predictions are also in qualitative agreement with the recycling current measurements shown in figure 3.

The qualitative agreement between the experimental measurements and the expected effects of the $\vec{E} \times \vec{B}$ drift on the EMC3-Eirene simulations strongly suggests that the $\vec{E} \times \vec{B}$ drift is a relevant transport mechanism that has to be included in

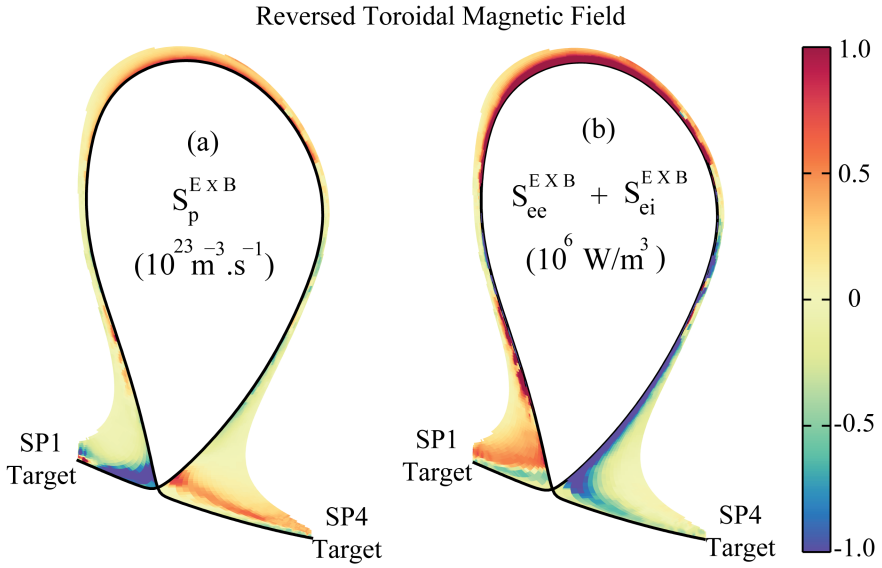

Figure 13. (a) Particle source, $S_{\mathrm{p}}^{\mathrm{E\times B}}$, and (b) energy source, $S_{\mathrm{e}}^{\mathrm{E\times B}}$, due to the $\vec{E} \times \vec{B}$ drift calculated using the EMC3-Eirene plasma density and temperature profiles for a SF+ configuration with $\sigma = 0.1$ and reversed B_ϕ.

future simulations of the SF divertor in order to obtain more meaningful, reliable and predictive results.

5. Summary

The potential advantages of the snowflake (SF) divertor to alleviate the divertor heat loads arise from its enhanced magnetic properties. Even though in TCV such enhancements are limited only to a narrow region of the SOL in the vicinity of the separatrix, significant changes of the plasma behaviour have been observed when the divertor configuration is varied from a standard single-null (SN) to a SF. Previous studies showed that these changes cannot be explained by the modified field line geometry of the SF configuration along with diffusive cross-field transport [22, 23], namely the power distribution among strike points (SPs) and the shape of the target profiles [22, 23]. This result strongly suggests the existence of an additional or enhanced cross-field transport in the null-point region of the SF divertor.

In this work, TCV experiments and numerical simulations of particle, momentum and energy transport using the EMC3-Eirene code are used to provide a better insight into the physical processes involved in the plasma transport in the TCV SF divertor. EMC3-Eirene simulations of the SF+ show that larger poloidal gradients of the kinetic profiles develop in the null-point region when the divertor configuration varies from a standard SN to a SF. These gradients generate a poloidal electric field in the null-point region of the SF+ configuration that is significantly larger than that in a SN configuration, thus having the potential of driving considerably larger $\vec{E} \times \vec{B}$ particle and heat fluxes in the edge of SF+ configurations. Assuming a constant plasma background,

these fluxes are estimated to be of the same order of magnitude of the particle fluxes calculated by EMC3-Eirene, specially in the null-point region. In a self-consistent model, however, the parallel particle flux would respond to this driven $\vec{E} \times \vec{B}$ flux causing significant changes in the kinetic profiles of plasma density and temperature. Since EMC3 does not take into account the effect of particle drifts, the approach described in this work has to be seen as the first step of an iterative process towards a self-consistent solution. However, the fact that this first step iteration changes the EMC3-Eirene results in the way that tends to minimize the discrepancy between simulations and experiments indicates that the $\vec{E} \times \vec{B}$ particle drift could be the missing element of the model to describe the experiments. For this reason, the $\vec{E} \times \vec{B}$ particle drift is thought to be responsible for the formation of the double-peaked particle and heat flux target profiles observed at SP1. The calculations also show that, in a SF+ configuration with forward toroidal magnetic field direction, the $\vec{E} \times \vec{B}$ drift convects particles from a region in front of the SP1 target and near the separatrix to a region more in the far-SOL, giving rise to the observed double-peaked target profiles. Comparisons between the simulations and the experiments in forward and reversed toroidal magnetic field directions further supports this conclusion. The formation of such a double-peaked profiles may have a beneficial effect on the divertor heat loads since they lead to broader target profiles and consequently lower peak heat fluxes. Note that although particle drifts are though to be an important transport mechanism in these discharges, they might not be the only missing element of the code and other effects caused by, for example, plasma-neutrals interaction and atomic processes might also be significant [39].

The results presented in this work strongly suggest that the additional cross-field transport required to explain the observed power distribution to SP3 is caused by the radial component of the $\vec{E} \times \vec{B}$ drift, which convects particles and heat across the SP4 leg into the PFR. This radial transport also explains the asymmetric shape of the particle and heat flux profiles measured at the SP3 target, in contrast to the symmetric profile shapes predicted by the EMC3-Eirene calculations. Furthermore, the results show that the smaller power distribution to SP3 observed at higher plasma densities is caused by a decrease of the poloidal gradients of the kinetic profiles in the null-point region, which leads to less $\vec{E} \times \vec{B}$ radial transport into the PFR. Due to the strong dependence of the parallel electron heat conductivity on the electron temperature [31], the same effect is expected to be observed in high power discharges since higher temperatures in the SOL lead to a substantial decrease of the poloidal gradients of the electron temperature and thus to a decrease of the $\vec{E} \times \vec{B}$ radial transport into the PFR.

In this work, the $\vec{E} \times \vec{B}$ drift is identified as an important transport mechanism in the edge plasma transport in the TCV SF+ configuration and, therefore, it has to be accounted in future numerical modelling in order to obtain more meaningful and reliable results.

Acknowledgements

This work was supported in part by the Swiss National Science Foundation. Discussions and suggestions from Prof. P Ricci and Dr. A Leonard are gratefully acknowledged. This work has been carried out within the framework of the EUROfusion Consortium and has received funding from the Euratom research and training programme 2014-2018 under grant agreement No 633053. The views and opinions expressed herein do not necessarily reflect those of the European Commission.

References

[1] H. Zohm *et al.*, Nuclear Fusion **53**, 073019 (2013)
[2] A. Loarte *et al.*, Nuclear Fusion **47** S203 (2007)
[3] M. Kotschenreuther *et al*, Physics of Plasmas **14**, 072502 (2007)
[4] D.D. Ryutov *et al.*, Physics of Plasmas **14**, 064502 (2007)
[5] D.D. Ryutov *et al.*, Fusion Energy 2008 (Proc. 22$^{\text{th}}$ Int. Conf. Geneva, 2008) (Vienna: IAEA) CD-ROM file IC/P4-8 `http://www-naweb.iaea.org/napc/physics/FEC/FEC2008/html/index.htm`
[6] D.D. Ryutov *et al.*, Plasma Physics and Controlled Fusion **54**, 124050 (2012)
[7] C.S. Pitcher and P.C. Stangeby, Plasma Physics and Controlled Fusion **39**, 779 (1997)
[8] F. Piras *et al.*, Plasma Physics and Controlled Fusion **51**, 055009 (2009)
[9] F. Piras *et al.*, Physical Review Letters **105**, 155003 (2010)
[10] V.A. Soukhanovskii *et al.*, Journal of Nuclear Materials **415**, S365 (2011)
[11] V.A. Soukhanovskii *et al.*, Physics of Plasmas **19**, 082504 (2012)
[12] V.A. Soukhanovskii *et al.*, Journal of Nuclear Materials **438**, S96 (2013)
[13] S.L. Allen *et al.*, 2012 Proc. 24$^{\text{th}}$ Int. Conf. on Fusion Energy (San Diego, 2012) PD/1-2 `http://www-naweb.iaea.org/napc/physics/FEC/FEC2012/index.htm`
[14] H. Reimerdes *et al.*, Plasma Physics and Controlled Fusion **55**, 124027 (2013)
[15] A.M. Runov *et al.*, Journal of Plasma Physics **72** 6, 1109-1112 (2006)
[16] Y. Feng *et al.*, Contributions to Plasma Physics **44** 57-69 (2004)
[17] Y. Feng *et al.*, Controlled Fusion and Plasma Physics: Proc. 27$^{\text{th}}$ EPS, Budapest, ECA Vol. 24B, 1188-1191, (2000)
[18] S.I. Braginskii, Reviews of Plasma Physics **1** 205-311 (1965)
[19] D. Reiter *et al.*, Fusion Science and Technology **47** 2, 172-186 (2005)
[20] Y. Feng *et al.*, Conference on Plasma Physics: 38$^{\text{th}}$ EPS, Strasbourg, P1.071
[21] D. Harting *et al.*, Journal of Nuclear Materials **415** S5404 (2011)
[22] G.P. Canal *et al.*, Conference on Plasma Physics: 55$^{\text{th}}$ APS, Denver **58**, PP8.46 (2013)
[23] T. Lunt *et al.*, Plasma Physics and Controlled Fusion **56**, 035009 (2014)
[24] B. Labit *et al.*, Conference on Plasma Physics: 39$^{\text{th}}$ EPS, Stockholm **ECA Vol. 36F**, P5.091 (2012)
[25] F. Hofmann, Computer Physics Communications **48**, 207-221 (1988)
[26] F. Hofmann and G. Tonetti, Nuclear Fusion **28**, 1871 (1988)
[27] R.D. Monk *et al.*, Journal of Nuclear Materials **241-243**, 396 (1997)
[28] A. Loarte *et al.*, Nuclear Fusion **38**, 331 (1998)
[29] A.V. Chankin *et al.*, Plasma Physics and Controlled Fusion **43**, 299 (2001)
[30] V. Rozhansky *et al.*, Nuclear Fusion **52**, 103017 (2012)
[31] P.C. Stangeby, *The Plasma Boundary of Magnetic Fusion Devices*, Institute of Physics Publishing, London (2000)
[32] A.V. Chankin *et al.*, Journal of Nuclear Materials **241-243**, 199 (1997)
[33] S.I. Krasheninnikov *et al.*, Physics of Plasma **2**, 2717 (1995)

[34] T.D. Rognlien *et al.*, Physics of Plasmas **6**, 1851 (1999)
[35] T.D. Rognlien *et al.*, Journal of Nuclear Materials **266-269**, 654 (1999)
[36] J.A. Boedo *et al.*, Physics of Plasmas **7**, 1075 (2000)
[37] M.J. Schaffer *et al.*, Journal of Nuclear Materials **290**, 530 (2001)
[38] J. Loizu *et al.*, Plasma Physics and Controlled Fusion **55**, 124019 (2013)
[39] L. Aho-Mantila *et al.*, 25$^{\text{th}}$ IAEA Int. Conf. on Fusion Energy (St. Petersburg, Russia, 2014) CD-ROM file TH/3-3